



Thermal modeling of electrically-pumped continuous-wave microring resonator-based topological insulator lasers

WEICHENG YOU,¹ SPARSH BALABADRAPATRUNI,^{1,2,3}
BRADLEY J. THOMPSON,² RICKY GIBSON,² 
SHAMSUL ARAFIN,^{1,*}  AND STEFAN C. BADESCU²

¹Department of Electrical and Computer Engineering, The Ohio State University, Columbus, Ohio 43210, USA

²Air Force Research Laboratory, Sensors Directorate, Wright-Patterson AFB, Ohio 45433, USA

³KBR, Inc., Beavercreek, Ohio 45431, USA

*arafin.1@osu.edu

Abstract: Deleterious effects caused by Joule heating in electrically-pumped continuous-wave InP-based topological insulator lasers based on two-dimensional microring resonator arrays are estimated in this theoretical study. Steady-state temperature distributions within such an array are developed using a full numerical solution. Thermal interactions between active gain regions and ring resonators pose significant operational and integration challenges, as these devices are extremely sensitive to temperature-induced changes in a material's index of refraction. Designing such an array benefits from clear understanding on the effects of systematic non-uniform heating profiles due to temperature variations among the rings. This paper first presents the thermal modeling of a single isolated ring under electrical pumping and then discusses its impact on an operational array composed of 10×10 such rings. The simulation results reported here were benchmarked against experimental measurements of the microring lasers, wherever possible. Calculations based on a tight-binding model for the array suggest that the laser exhibits single-mode optical output with the preservation of topological properties up to 4 times the threshold current. The useful operating range of the array is mainly limited by the thermal shifts of wavelengths in addition to the wavelength disorders due to fabrication imperfections.

© 2024 Optica Publishing Group under the terms of the [Optica Open Access Publishing Agreement](#)

1. Introduction

Topological insulators behave as insulators in their interior but as conductors in their surface edges. What is particularly remarkable is that surface current traversing conducting edge states is forced to exclusively move in a single direction with no backscattering in the opposite direction, and immune to both perturbations as well as disorders. These unique features of the material enable the applications of spintronic and electronic devices utilizing its quantum transport. The field of optoelectronics has recently realized the potential of topological material by emulating its properties in a tailored optical cavity [1–3]. This allows manipulating light in a manner that is analogous to manipulating the flow of spins/electrons in the spintronic and electronic devices. Hence the idea of physically realizing topological insulator diode lasers (concisely topological lasers) emerges.

The development of advanced lasers with improved performance, robustness, and energy efficiency has been a driving force in the field of photonics. Traditional laser designs often face challenges, such as sensitivity to defects, backscattering, and feedback, which degrade performance and limit applications. In this context, the emerging field of topological lasers offers a novel and promising approach to address these challenges. For instance, electrically-pumped (EP) and continuous-wave (CW) high-brightness laser sources emitting at $1.55 \mu\text{m}$ with good

optical isolation are of particular interest for applications such as light detection and ranging (LiDAR) [4–6], seed lasers for optical amplification [7,8], and optical communications [9–12]. Especially for communication applications, a single-mode output power in the ≥ 1 W range of the master oscillator is a clear advantage, as fewer, or even no subsequent power amplifier stages will be required. The topological laser technology holds the promise of providing high brightness in a compact package that will enable these applications as they offer simultaneously reasonably good on-chip output power with inherent optical isolation [13,14].

Topological lasers emulate the quantum Hall Effect (QHE) based on a synthetic gauge field resulting from the judicious shifting of the ‘link’ elements between the site resonators of an array. This, in turn, creates a non-trivial topological phase which is utilized to force all rings in the array to act as a single phase-locked laser. The topological array emits at a single frequency via constructive interference among individual array elements, suggesting that the emitters are mutually coherent. Employing topological insulator ring arrays where each ring within the array emits light in-plane, and the coupling between the emitters in the topological platform facilitates coherent emission of the whole array, enables output power scaling. For instance, a 40×40 array can behave as a single coherent light source, paving the way for large-scale, high-brightness semiconductor lasers, equivalent to 156 phase-locked ring lasers around the perimeter, operating as one from a single chip [15]. This is an avenue to make arrays of miniature lasers work together as one: a single highly-coherent high-brightness laser.

One of the primary challenges in using microring resonators is their extreme sensitivity to refractive index changes. Hence, both fabrication disorders, and thermal variations, referred to as “thermal systematic shifts,” give rise to the shifts of ring resonances from their designed value in an array. Fabrication disorder refers to unwanted defects that occur during processes such as lithography and plasma etching, leading to a uniform distribution of resonances across the entire array. On the other hand, thermal shifts, which result from current pumping at edge, primarily causes a redshift in edge ring resonances compared to the bulk, with smaller redshifts observed in nearest neighbors, next-nearest neighbors, and so on. Due to a large thermal impedance from small-area ring devices and such thermal variations, in particular, CW operation of topological lasers at room temperature remains unachieved. Joule heating during CW pumping at the edge rings exacerbates the wavelength shift of the individual microrings throughout the array, consequently degrading the laser’s performance. Despite topological lasers being expected to show remarkable practical resilience against such disorder, there is a limit in a finite-sized array to the strength of the overall disorder that could be sustained.

To date, topological lasing has been successfully achieved in both optically- and electrically-pumped in one-dimensional (1D) Su-Schrieffer-Heeger resonator arrays [16–19] and two-dimensional (2D) arrays [20–24]. However, there was no edge transport in 1D systems, hence no protection against onsite disorder, and the lasing was almost fully confined to a single resonator. 2D topological lasers employ active lattices that exhibit quantum Hall, quantum spin Hall, or valley Hall effects, with or without the application of external magnetic fields. The first optically-pumped ring-based topological lasers were demonstrated using the InP-based material platform [20] and it displayed all the expected features. This laser was constructed on a standard optoelectronic platform, as an aperiodic array of 10×10 coupled ring-resonators for $1.55 \mu\text{m}$ emission. Very recently, EP topological lasers based on ring arrays with $30 \mu\text{m}$ diameter under pulsed conditions with a 15 ns pulse width and low duty cycle (0.4%) at $1.55 \mu\text{m}$ have been reported [24]. However, the devices exhibited poor performance in terms of low optical output power (reported in arbitrary units) which limits their suitability in the aforementioned applications. In 2022, room-temperature CW operating EP lasers were demonstrated using two $50 \mu\text{m}$ diameter coupled microrings based on InAlGaAs system, achieving injection currents up to 50 mA [25]. Other studies highlighted a separate finding, indicating that a single microring device with a diameter of $30 \mu\text{m}$ could achieve CW lasing at temperatures as high as 90°C [26,27]. This

result suggests the feasibility of employing EP and CW topological lasers based on a ring array configuration.

In this study, we conduct a comprehensive investigation of thermally-induced effects in InP-based topological insulator lasers by considering that they are EP and CW-operated. Our analysis encompasses a thorough examination of the thermal characteristics of the topological laser system, including the variations of the energy distribution and power spectral density of lasing modes. We employed both analytical and numerical methods to provide deeper understanding of the thermal effects on the performance and stability of the topological insulator laser. Our findings have significant implications for the development of robust and efficient topological insulator lasers, paving the way for their widespread applications in a variety of fields.

2. Electrical modeling

The design of microring resonator-based EP topological lasers utilize an InGaAsP/InP laser structure. Figure 1(a) shows the schematic of the epitaxial laser structure. Layer structure details can be found elsewhere [20]. Ring waveguides with $15\ \mu\text{m}$ radii and $1.4\ \mu\text{m}$ ridge widths are considered in this study. The choice of $1.4\ \mu\text{m}$ is to ensure single spatial mode operation and the proper evanescent mode coupling between the adjacent rings. A smaller width of the ring enhances the coupling efficiency, benefiting the topological property. However, the smaller dimensions increase the fabrication difficulties. The choice of the ring radii mainly depends on the bend loss and propagating mode in the waveguide. We want the smallest sustainable radii to maximize the free spectral range (FSR). We also found that the TM mode becomes dominant when the ring radius is less than $11\ \mu\text{m}$, which increases the propagation loss. In this work, a commercial finite difference eigenmode (FDE) solver [28] was used to determine the change in effective refractive index n_{eff} , group refractive index n_g , and use a 1D gain solver utilizing the $k \cdot p$ method to get the optical gain and optical transparency at different temperatures. This ultimately allowed us to estimate the light-current-voltage ($L-I-V$) curve and wavelength tuning with temperature of a single microring laser by a traveling wave laser model.

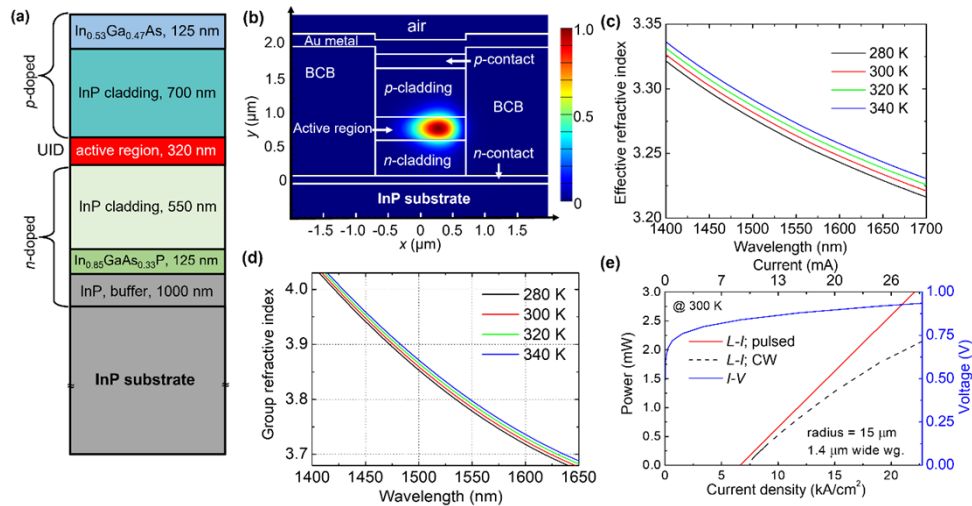


Fig. 1. (a) Schematic cross-section of the InP-based epitaxial layer structure under study; The simulation model of a single microring laser. (b) Cross-section of a $15\ \mu\text{m}$ radius microring laser structure with 2D surface plot of the light intensity of the fundamental transverse mode. (c-d) Effective and group refractive index at different temperatures; and (e) numerically calculated output characteristics under CW and pulsed operations, as well as operation voltage versus current for the laser devices.

A 2D finite difference Eigenmode solver [28] was used to perform mode simulations on the cross-section of ring waveguides by utilizing the complex refractive indices of the epitaxial layers. Figure 1(b) displays the 2D optical intensity distribution of the fundamental transverse electric (TE) mode in the 1.4 μm wide laser waveguide structure with a 15 μm bend radius. Without the separate confinement heterostructure (SCH) layers, the optical confinement factor Γ in multi-quantum well (MQW) based active region is calculated to be 60.1%. With the use of thinner cladding on both p - and n -sides, the calculated Γ in the p - and n -contact layers are 0.5% and 0.07% which are larger compared to a typical laser structure [29]. For the ease of fabrication, the laser structure with relatively thin cladding and no SCH layers is considered in our study, which results in lower optical confinement and higher optical loss.

The refractive indices of each epitaxial layer are temperature dependent and change at a different rate [30–33]. The effective index and group index of the fundamental TE mode versus wavelength at different temperatures are shown in Figs. 1(c) and (d). The calculated effective and group index change with temperature by $2 \times 10^{-4}/\text{K}$ and $4.8 \times 10^{-2}/\text{K}$, respectively. These changes of refractive indices affect the resonance condition of the microring and thus alter the final emission wavelength. Due to the weak temperature dependence of the material's refractive indices, a negligible change of the confinement factors with temperature is found, hence the optical coupling between each ring was considered as constant. The simulation of the gain medium was conducted using a 1D physics-based gain solver [28], which performed a $4 \times 4 k.p.$ calculation to determine the stimulated and spontaneous emission in the MQW gain medium. Considering the large barrier separation, the QWs were treated as uncoupled, allowing calculations for a single QW to expedite the simulation process. Once completed, the outcomes were scaled to represent the total number of QWs. We then extracted the transparency density and differential gain from the gain simulation which was used to set Lorentzian gain parameters in the traveling wave laser model simulation to determine the output power and emitted spectrum of the single microring laser. The calculated L - I - V characteristics are shown in Fig. 1(e). To construct the CW L - I characteristics, Joule heating in the device was considered. The calculated CW threshold current density is at $\sim 6 \text{ kA}/\text{cm}^2$ (corresponding to 8 mA current) with 0.83 V applied voltage for an isothermal case.

3. Thermal modeling

In order to understand the temperature-dependent optical properties of a single ring laser, the lasing spectra of the devices were then calculated. Figure 2(a) presents the simulated lasing spectra of a single-ring laser at various heatsink temperatures. The simulation was performed by considering that the devices were pumped under pulsed conditions with a low duty cycle and hence, we ignored Joule heating. This means that the internal temperature of the device is the same as the heatsink. This does not hold true for the ring lasers operating in CW. The CW-operating devices heat up with applied electrical power due to Joule heating and as a result, the device's internal temperature is higher than the heatsink temperature. The peak wavelength shows an almost linear relationship with heatsink temperature, as illustrated by the black line in Fig. 2(b). With every 1 K increment in temperature, the peak wavelength undergoes an approximate shift of 0.08 nm. The thermal tunability of the EP ring devices was also experimentally measured under pulsed conditions by varying the heatsink temperature at a constant electrical power as shown by the blue line in Fig. 2(b). The thermal tuning rate matches well with our simulated results.

3.1. Single ring-level simulation

To assess the thermal shifts of topological lasers, it is important to explore device mounting options, i.e., how a single isolated ring is attached to its heatsink ultimately determines its thermal management. The traditional and most commonly used option to mount lasers is epitaxial-side-up (epi-up) geometry. However, from the thermal performance standpoint, the epi-up geometry is

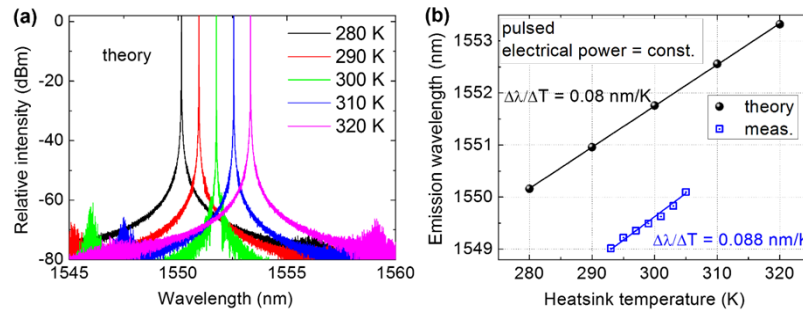


Fig. 2. (a) Spectra of single microring laser by varying heatsink temperature at a constant pulsed driving current of 12 mA; and (b) temperature-dependent wavelength variation by both theory and experiment.

undesirable since this option leaves InP substrate material with low thermal conductivity of 68 W/m-K between the active region and the heatsink. Importantly, this low thermally-conductive material is roughly two orders of magnitude thicker than the case of the epitaxial-side-down (epi-down) geometry, thus increasing the thermal resistance between the active region and the heatsink. Figures 3(a) and (d) show the 3D schematic of a fully-processed single isolated ring with the two mounting methods that require standard device fabrication. Dry etching is first needed to define rings with the aforementioned dimensions. We considered etched sidewalls of the rings to be passivated with 200-nm-thick plasma-enhanced chemical vapor deposited Si_3N_4 . BCB planarization process is required to electrically isolate co-planar top *p*- and bottom *n*-contacts. The multi-quantum well (MQW) region primarily determines the waveguiding and the optical mode is confined in this active region.

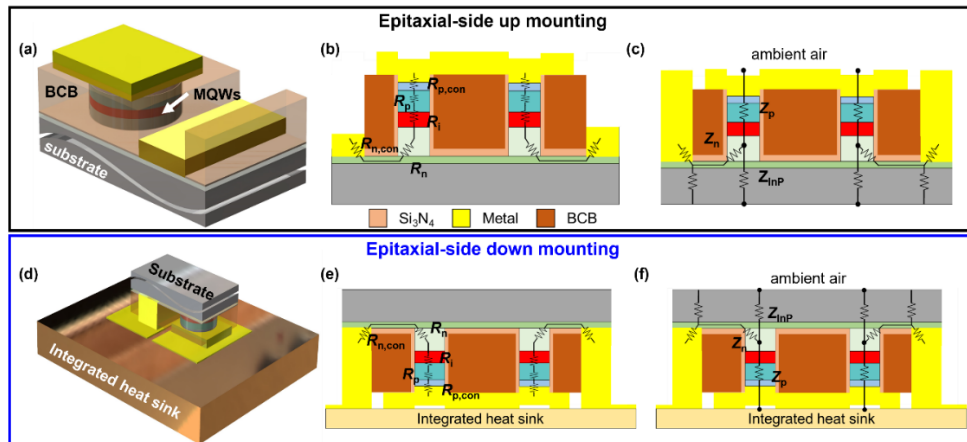


Fig. 3. (a) and (d) 3D schematic views of a fully-processed electrically-pumped microring laser; (b) and (e) Cross-sections of the single microring laser with electrical resistance model; (c) and (f) Thermal resistance model, with epi-up and epi-down designs.

Electrical impedances of several parts of the ring lasers, contributing to inevitable Joule heating after applying CW current, are determined by simulations from a 3D commercial device solver [34]. Due to increased resistive heating, a high Q factor, and a reduced cavity volume, the resonance wavelength of the microring resonators exhibit significant sensitivity to thermal effects during the CW pumping. The equivalent electrical resistance model of the microring

laser cross-section is shown in Figs. 3(b) and (e). During CW operation, Joule heating was introduced by contact resistance ($R_{n,\text{cont}}$, $R_{p,\text{cont}}$), cladding resistance (R_p , R_n), and intrinsic layer resistance (R_i). Table 1 lists the simulated resistance values based on the doping concentration of each region by the commercial solver and literature [26]. The relatively higher resistance in the p -doped region than in the n -doped region is due to the lower mobility of holes. The series resistance value varies with device geometry and doping concentration. In this analysis, we have not accounted for the boundary electrical resistance between each layer for the simplified model. In practical applications, the multi-layered system presents more intricate heat transmission dynamics, often leading to increased electrical impedance. This complexity stems from factors such as the surface treatment process and various deposition techniques.

Table 1. Resistance components of the proposed microring laser

Components		Resistance (Ω)
p -doped	$R_{p,\text{cont}}$	2.5
	R_p	2.8
Intrinsic UID	R_i	7.1
n -doped	$R_{n,\text{cont}}$	3.2
	R_n	0.14

Figures 3(c) and (f) show the simplified equivalent thermal impedance models, specifically for the epi-up and epi-down mounted devices, in which Z_n , Z_p , and Z_{InP} represent the thermal impedance associated with heat transmission through p mesa, InP substrate, and n -contact layer, respectively. Due to the low thermal conductivity of the BCB layer, we ignored the path of ring-BCB-air for thermal dissipation. The different mounting designs correspond to variations in the relative distances between the heat source and the heatsink. Due to less heat dissipation efficiency to ambient air, the majority of the generated Joule heat must be dissipated to the heat sink. The epi-down design facilitates heat transfer directly to the heat sink, bypassing the thick InP substrate. This approach has a significant impact on the heat flux and leads to a substantial reduction in the overall thermal impedance.

The heat transfer analysis within the laser devices was numerically simulated using a commercial 3D finite element modeling tool [35], as shown in Fig. 4. Tetrahedral Meshing convergence tests are performed in order to select proper mesh element sizes. The mesh element sizes were non-uniformly varied near the critical components of the ring structures including active region and coupling regions. The minimum and maximum meshes are 5 nm and 9.25 μm , and the minimum element quality and average element quality are 0.43 and 0.89, respectively, which are sufficient for this particular simulation [36]. Due to these finer mesh sizes, a negligible change in percentage errors was found to be $<0.01\%$. The thermal properties of the materials utilized in the microring structure are presented in Table 2. To calculate the thermal properties of ternary and quaternary alloys, we employed Vegard's law. The characteristics of the active region are determined to be the geometric average of the QWs and barriers. Compared to most semiconductor materials, gold exhibits a much higher thermal conductivity. Conversely, the dielectric and polymer materials used in photonics tend to have subpar thermal performance.

The two mounting architectures are considered and compared in Fig. 4 as part of the investigation of thermal management within the ring devices. For both the designs, we set a constant temperature at the device bottom as a boundary condition, symbolizing an ideal heatsink and the heat source is the Joule heating generated by relevant current flow through the resistance from Table 1. In epi-up mounting, represented in Figs. 4(a) and (b). This configuration results in an approximately 4°C increase in the active region temperature with respect to the heatsink when an injection current density of 18.2 kA/cm^2 (which is 24 mA injection current) is applied. This $3 \times I_{\text{th}}$ injection current is a reasonable operating current during CW pumping, and different

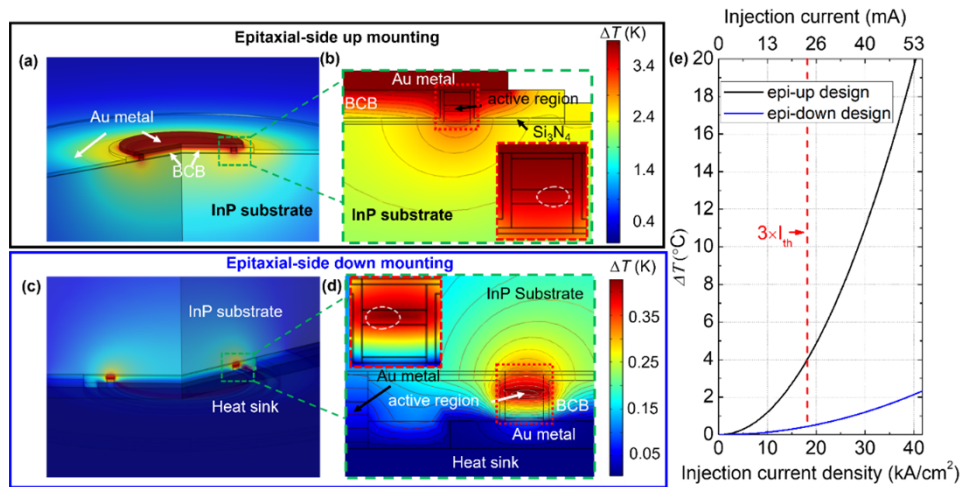


Fig. 4. Cross-sectional views of the microring lasers and the simulated temperature contour. (a) and (c) are cutaways of a 3D heat simulation of epi-up and epi-down mounting; (b) and (d) are cross-sections through one side of epi-up and epi-down mounting. The white circles in the insets show the simulated light intensity of the fundamental transverse mode where 80% of the light is confined. All results were simulated at 18.2 kA/cm^2 (24 mA) injection current density. The color legends have different temperature scales in each case; (e) Temperature changes at the laser active region with different injection currents corresponding to the two mounting methods

Table 2. Thermal properties of selective constituent materials for the rings at 20°C

Materials	Thermal conductivity $\text{W}/(\text{m}\cdot\text{K})$	Density kg/m^3	Heat capacity $\text{J}/(\text{kg}\cdot\text{K})$
InP	68	4810	310
Active region	45.7	5356.8	392
Gold	316	19300	129
BCB	0.29	957	2.18
Si_3N_4	18.5	787	3100
<i>n</i> -contact	57.3	4998	412.5
<i>p</i> -contact	72.2	4495	461

injection currents are also shown in the following sections. In contrast, in epi-down mounting, depicted in Figs. 4(c) and (d), heat generated in the active region dissipates directly to the heat sink through the metal contacts, avoiding the impedance of the thick substrate. This improved design shows the temperature rise $\Delta T = 0.47^\circ\text{C}$ with respect to the heat sink. However, the epi-down approach demands high-precision flip-chip bonding and alignment, which not only consumes more labor time but also poses challenges in integrating additional photonic components. Note that most of the fundamental transverse modes are confined within the active region, exhibiting a uniform temperature distribution. This is illustrated by the white circles in the insets of Figs. 4(b) and (d). This suggests that the average temperature change within the active region is accurate enough to capture thermal dynamics even as the active region is heating up more than other layers during the CW pumping.

When simulating a device with small dimensions, these reflected heat waves distort the heat distribution, resulting in inaccurate configurations. Hence, for the purpose of these simulations,

we accounted for a circular substrate area (in-plane) of $500\ \mu\text{m}$. It should be noted that the thickness of the InP substrate was consistently maintained at $150\ \mu\text{m}$. The average temperatures of active region for both the designs are shown in Fig. 4(e). The average temperature was calculated by taking the mean from three different planes. These planes are located at the midpoint of the $320\ \text{nm}$ thick active region, and $80\ \text{nm}$ above and below that midpoint. The overall impedances for the epi-up and epi-down designs with the proposed dimensions are $450^\circ\text{C}/\text{W}$ and $49^\circ\text{C}/\text{W}$, respectively. We then applied the wavelength thermal tuning to each microring in an array as an input to a tight-binding model in order to determine the figure of merit for topological edge mode for temperature distribution and some nominal values of fabrication disorder.

3.2. Ring array simulation

Figure 5(a) illustrates the proposed EP 10×10 TIL array. Our simulations have demonstrated that a 5×5 array, at the very least, is necessary to exhibit the topological property. A smaller array exhibits trivial propagation. Therefore, our choice with the 10×10 array is reasonable and facilitates the observation of topological transportation more effectively than a smaller array. Furthermore, a 10×10 array provides the representative behavior of the ‘outer shell’ shifting relative to the bulk while the center of the array remains essentially unperturbed. Any larger arrays experience a higher percentage of the bulk with an essentially unperturbed temperature/wavelength resonance. Hence, the 10×10 array is sufficient to explore when delocalization occurs at the outer shell. The electrodes exclusively cover and pump the edge rings. Consequently, only these edge rings produce Joule heating during operation. The generated heat flux at the pumped rings dissipates to neighboring rings, resulting in a thermal gradient across the array. This temperature gradient alters the wavelength dispersion of each ring, leading to non-uniform heating profiles in the topological array. As a result, the capacity of EP TILs to counteract the disorders is constrained by these thermal effects. To obtain a thorough understanding of TILs, we present a comprehensive thermal analysis using a heat dissipation model by the commercial 3D finite element solver. By employing the three-dimensional steady-state heat transfer model, we extracted the internal temperature distribution of the topological array.

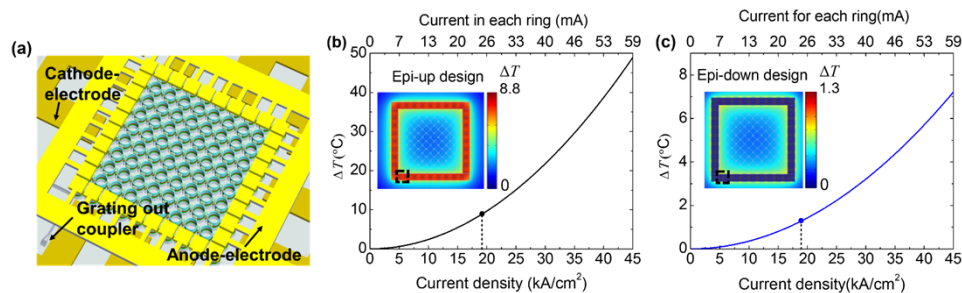


Fig. 5. (a) 3D schematic view of a fully-processed electrically-pumped topological insulator laser; The highest temperature changes at the laser active region of the ring in the array (which is circled in the insets) with different injection current corresponding to the (b) Epi-up-; (c)Epi-down mounting designs (Please note that in the epi-down design (see (c)) where the device is attached to an integrated heat sink not shown, the highest temperature in the active region cannot be seen in the top-view inset).

In these two models, most of the heat dissipates to the bottom (epi-up) or top (epi-down) heat sink which is constant at $293\ \text{K}$, and the rest of the heat is transferred to the air by radiation and natural convection through layers exposed to the air. By arranging the single rings and selectively injecting current on the edge rings, rings within the array are heated up non-uniformly due to Joule heating. Figures 5(b) and (c) show the temperature of the ring with the highest change in

the topological array at different injection currents. The largest injection current density shown here is about 7 times the threshold. For real applications, the laser hardly survives at such a high injection. If we consider 3 times higher than the threshold which is around 18.2 kA/cm^2 , the insets in Figs. 5(b) and (c) show the top view of the thermal distribution at $3 \times I_{\text{th}}$ current and the maximum thermal wavelength shift difference of the ring within the array is about 0.7 nm which is high enough to affect the topological property of the array. In the epi-down mounting, the maximum wavelength shift under this pump condition is less than 0.1 nm, which means the topological property will less likely impact under this type of heat dissipation configuration.

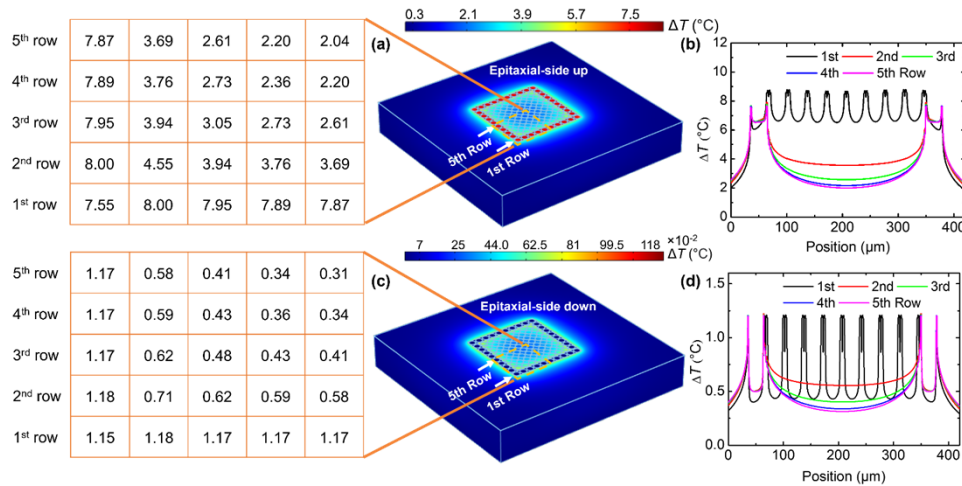


Fig. 6. The thermal simulation model of topological laser array. (a) and (c) The heat distribution when pumping at $3 \times I_{\text{th}}$ with the epi-up and epi-down designs. The substrate bottom and top are maintained at a temperature of 293 K by heat sinks (not shown) whose dimension is large compared to the device dimensions; and (b) and (d) temperature rise at each row in the arrays; The tables on the left show the average increased temperatures of each ring at the pumping current.

Figures 6(a) and (c) depict the temperature distribution of epi-up and epi-down mounting of the TILs, respectively, with an injection current density of 18.2 kA/cm^2 . The heat sinks are not shown in the figures. In this simulation, we ignored the optical output coupler for the simplified and symmetrical model. The left table presents the increased temperature in each ring within the eighth of the array. Due to the symmetric property, we easily determined the temperature mapping of the entire array. The increased temperature proportion mapping for each ring in the array will not change due to the same thermal dissipation and properties of the materials, which means the whole thermal distribution can be determined once we know the temperature increase of any of one ring in the array. One thing to note is that the ring in row 1, column 2 shows the highest increase in temperature. This is due to the greater number of nearest neighbors being pumped of this certain ring. The rings at the edges of the array were considered as heat sources, generating heat for the surrounding area. In contrast, the middle ring in the array receives less impact from the edge rings, so it shows a lower temperature. The lowest temperature increase is around one-quarter of the highest value which means only about a quarter of the wavelength shift in the innermost ring compared to the edge rings. A higher injection current induces a higher wavelength shift in the TIL array. This observation highlights the significance of temperature effects on the laser's performance and indicates the possibility to destroy the topological property of the array. Figures 6(b) and (d) show the 1D temperature increase of each row in the array.

4. Topological property modeling

The tight-binding approach from solid state physics is the simplest approach that captures the main physics of topological laser arrays [1,20,21,24,37,38]. In this formalism, the ring resonators (instead of atoms) at sites m, n are represented by their on-site resonance energies $\varepsilon_{m,n}$, and they are coupled only to their nearest neighbors by hopping parameters J . For a finite array, the topological gap was populated by surface states whereas the broad density of states was populated by bulk states. In arrays that are finite in both directions, as it is the case in fabrication and experiment, the wavenumber was not defined, and the photonic bands are replaced by density of states energy and chirality as proper quantum numbers. The topological invariants of our laser systems were not defined in our study due to the finite dimensions in all directions. Instead, a local invariant can be defined in a finite system using real space techniques rather than the Berry phase [39] which will be shown in our follow up paper.

In an ideal lattice, all the resonators have the same energy ε , which can be taken as the reference. In the simplest descriptions [1,20,21] the energy scale is given by a uniform hopping parameter J , and all other parameters are given relative J . In a realistic system, there is an inherent resonance disorder in resonator frequencies due to fabrication imperfections [1,21]. We account for the distribution of resonances by a Gaussian model with a standard deviation σ_U . It was shown that the topological states in passive systems are present for disorder levels up to Gaussian distribution widths $\sigma \approx J$ [1] and that was also claimed for topological lasers [20,21].

In order to describe the pumped system, we used an adaptive fifth-order Runge Kutta integration algorithm with a fourth-order predictor-corrector method. This approach is found to converge even for higher levels of disorder and pumping power, when the system may exhibit multimode lasing. One main difference between this work and previous theoretical and experimental works [21,37] is that thermal effects produce a very large systematic shift of resonances in one direction. For large currents, the outer shell of rings shifts from the next shell by more than the coupling parameter J . In these cases, the outer shell is essentially decoupled and becomes a unidirectional chain of resonators. This point suggests the need for thermal management in the EP arrays.

As shown in Fig. 5 and 6, the thermal shift in the epi-up design is significantly higher and hence, such devices easily exceed the hopping parameter J and destroy the topological property. Therefore, we focused only on the epi-down mounted device and its operating range during electrical pumping was calculated. We define the degree of mode localization on the boundary by the relative weight $W_B = \sum_{\text{perimeter}} |E_i|^2 / \sum_{\text{array}} |E_i|^2$, and the emitting modes length is the number of the light emitted cavities on the perimeter of the array. Topological modes have a strong localization on the outer shell of the array. On the other hand, very large thermal shifts of the ring resonators potentially change the array topology close to the boundary. To describe the laser operation, we considered pumping currents in the range [0, 50]mA and ring disorder strengths $2\sigma_U$ in the range [0, 2J]. We assumed that the temperature changes are a result of electrical current-induced Joule heating, and we take into account the corresponding change in the material's refractive index, which leads to a change in emission wavelengths. As a matter of fact, the change in emission with temperature is linear and our experimental results for a single ring (Fig. 2(b)) show that the change of wavelengths with the temperature occurs a constant rate. Hence the change of wavelengths with temperature in the ring devices exhibits a systematic behavior. For reference, we first considered the modes in a model of heated lattice which has thermal shifts but neglecting the current pumping. In this configuration, we ignored higher order saturation terms in the laser dynamics equation and transferred this laser system to an eigenvalue problem. All the allowable modes were calculated in this passive system. We considered the 10 modes with the highest edge localization W_B . We ordered these modes in descending order of their energies. The spectra are shown in Figs. 7(a-b) for a disordered system with $2\sigma_U = 0.25J$ and $2\sigma_U = 1.0J$, respectively. For the less disorder case, these modes have better defined energy separations than the larger disorder. At low currents, both the modes fall within both topological

bandgaps, characteristic to topological modes. As the current increases, the whole spectrum red shifts, and eventually these localized modes end up entirely within the lower topological bandgap. The error bars in this figure represent the random disorder $2\sigma_U$ caused energy spreading for each calculation. It is important to note that if the modes shift into the bulk band, the energy of the mode can be distributed anywhere within the bulk band, resulting in significantly greater energy uncertainty.

In the second part of modeling, we looked at the lattice with electrical pumping. We looked at the time dependence of the total power in the steady oscillatory state and performed a power spectral density (PSD) analysis. For low disorder levels, the system oscillates in a single mode which coincides with a mode of the heated but unpumped lattice. For high disorder levels, especially at high currents, the system has a multi-mode oscillation. We considered statistical ensembles for different disorder levels. Each ensemble consists in 500 different realizations of a

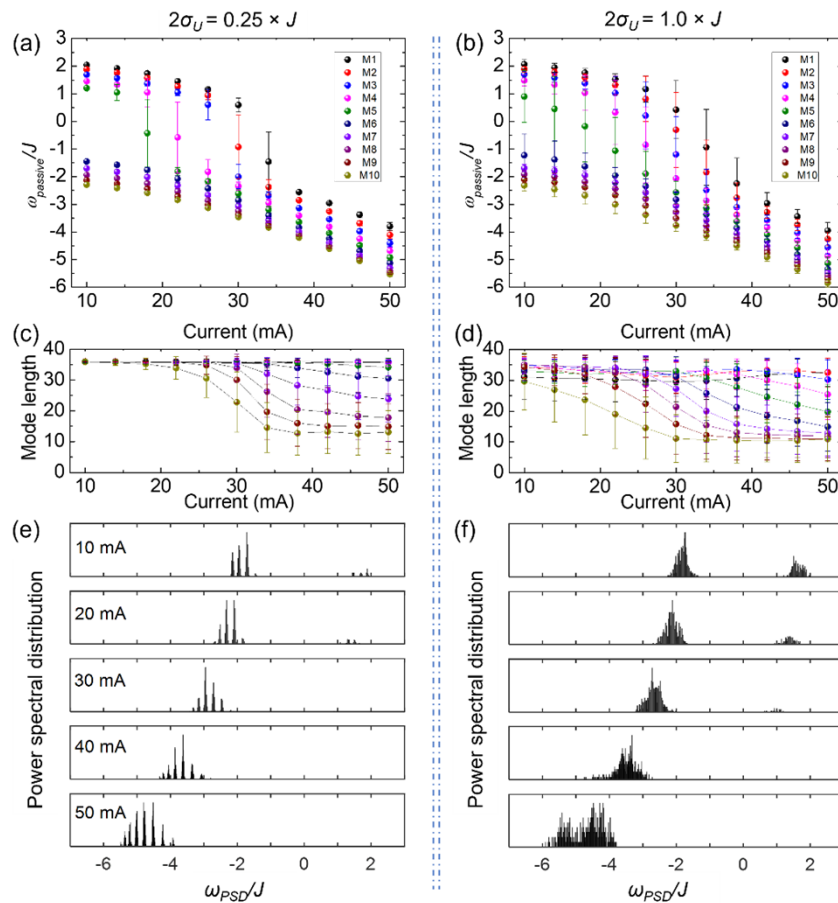


Fig. 7. (a-b) Energies of the top 10 modes with the highest periphery localization for a system with $2\sigma_U = 0.25J$ and $2\sigma_U = 1.0J$ as a function of pumping current. (c-d) The localization mode lengths of the top ten modes on the periphery of the array with $2\sigma_U = 0.25J$ and $2\sigma_U = 1.0J$, and the color code identifies the same modes as in (a-b). The less length means the more weight of the certain mode penetrates to the bulk region of the array and behave the more trivial property. (e-f) The comparison between power spectral density statistics for a low level of disorder $2\sigma_U = 0.25J$ and a larger disorder $2\sigma_U = 1.0J$, for increasing currents. All simulations are done with epi-down design.

disorder level $2\sigma_U$. In Figs. 7(e) and Figs. 7(f), we compare statistics for a low level of disorder $2\sigma_U = 0.25J$, with those for a larger disorder $2\sigma_U = 1.0J$, for increasing currents. Figures 7(e) show how the PSD lasing lines group around modes of the unpumped array, with the largest probabilities in the middle of the topological bandgaps. All of these emitting modes have very similar values of W_B around 0.90. The length of the emitting modes is lowered from 36 to ~ 25 sites as the current increases (Fig. 7(c)). In the shorter length case, the outer rings essentially decouple from the center of the array due to the large wavelength deviation, forming essentially a non-topological chain. The periphery modes lose topological character and therefore are affected more by disorder, which reduces their length. Figure 7(f) show a broadening of these statistical distributions, where modes are essentially anywhere in the topological bandgap. In this case the system has multimode operation above 30 mA more often than the case of small disorder and the histograms show the intensity of the highest PSD peak for each disorder realization. As shown in Fig. 7(d), the number of emitting rings on the perimeter reduces to an average of 10 sites for this disorder.

These effects are further enhanced by larger disorder levels, where we observe less deterministic behavior (broad histograms) and a reduction in output power even at low thermal bias. This is consistent with the findings in [21]. Further, at high currents the emitting modes become localized to a few sites, losing completely the topological character. Hence, intense CW electrical pumping results in thermal shifts that distort the energy spectrum of these arrays. For large shifts, the perimeter rings form essentially a unidimensional chain that gives rise to non-topological modes which are strongly affected by disorder. With the parameters in our model, the epi-down system operates in a topological manner up to ~ 35 mA for disorder $2\sigma_U \leq J$ which is around 4 times the threshold current. This model shows that in order to realize a CW EP topological laser the effect of thermal shifts have to be mitigated. One possible way to achieve that is to increase the value of the coupling constant J , which reduces at the same time the effect of fabrication disorder.

5. Conclusions

In conclusion, our modeling highlights the importance of thermal effects in topological lasers. These lasers, composed of arrays of ring resonators, are pumped on the edges of the array to avoid lasing in disordered bulk rings. This edge pumping leads to strong, systematic shifts of laser resonances, consequently causing the decoupling of outer shells from the internal shells of the arrays, changing the topology necessary for topological modes. When pumping levels remain moderate, thermal shifts and fabrication disorder collaboratively induce mode localization which limit the transport of energy around the array cavity. The advantage of electrical pumping for integration is limited or precluded if a mitigation of resonance thermal shifts is not implemented. Thermal management in the ring-based lasers could be improved using several methods such as shunt design [27], double shunt [26] and double heat sinks [40]. Despite the small footprint of our rings with $1.4 \mu\text{m}$ width and their closely-packed arrangement as an array, one could adopt these approaches to alleviate the heating issue of edge-rings.

Funding. Office of the Secretary of Defense.

Acknowledgments. The authors gratefully acknowledge support from the Applied Research for the Advancement of S&T Priorities program of the Office of the Under Secretary of Defense

Disclosures. The authors declare no conflicts of interest.

Data availability. Data underlying the results presented in this paper are not publicly available at this time but may be obtained from the authors upon reasonable request.

References

1. M. Hafezi, E. A. Demler, M. D. Lukin, *et al.*, "Robust optical delay lines with topological protection," *Nat. Phys.* **7**(11), 907–912 (2011).
2. M. Hafezi, S. Mittal, J. Fan, *et al.*, "Imaging topological edge states in silicon photonics," *Nat. Photonics* **7**(12), 1001–1005 (2013).
3. M. Hafezi, "Synthetic gauge fields with photons," *Int. J. Mod. Phys. B* **28**(02), 1441002 (2014).
4. Z.-J. Han, X. Tang, Z.-M. Wu, *et al.*, "A real-time and anti-interference lidar based on field programmable gate array," in *2021 19th International Conference on Optical Communications and Networks (ICOON)*, (IEEE, 2021), 1–3.
5. Q. Hu, P. J. Rodrigo, and C. Pedersen, "Remote wind sensing with a CW diode laser lidar beyond the coherence regime," *Opt. Lett.* **39**(16), 4875–4878 (2014).
6. P. J. Rodrigo, T. F. Iversen, Q. Hu, *et al.*, "Diode laser lidar wind velocity sensor using a liquid-crystal retarder for non-mechanical beam-steering," *Opt. Express* **22**(22), 26674–26679 (2014).
7. A. Gourevitch, G. Belenky, L. Shterengas, *et al.*, "1.5 and 2.3 μm diode laser arrays for optical pumping," in *Lidar Remote Sensing for Environmental Monitoring VI*, (SPIE, 2005), 239–246.
8. F. Lelarge, B. Dagens, J. Renaudier, *et al.*, "Recent advances on InAs/InP quantum dash based semiconductor lasers and optical amplifiers operating at 1.55 μm ," *IEEE J. Sel. Top. Quantum Electron.* **13**(1), 111–124 (2007).
9. S. Ishimura, R. Morita, T. Inoue, *et al.*, "Proposal and demonstration of free-space optical communication using photonic crystal surface-emitting lasers," *J. Lightwave Technol.* **41**(12), 3688–3694 (2023).
10. T. Katsuyama, "Development of semiconductor laser for optical communication," *SEI Tech. Rev.* **69**, 13–20 (2009).
11. Y. Mao, Y. Cheng, B. Xu, *et al.*, "Record-high power 1.55- μm distributed feedback laser diodes for optical communication," in *Optical Fiber Communication Conference*, (Optica Publishing Group, 2021), W1B. 7.
12. Y. Xu, T. Fu, J. Fan, *et al.*, "High-power supersymmetric semiconductor laser with a narrow linewidth," in *Photonics*, (MDPI, 2023), 238.
13. K. Fang, Z. Yu, and S. Fan, "Realizing effective magnetic field for photons by controlling the phase of dynamic modulation," *Nat. Photonics* **6**(11), 782–787 (2012).
14. M. Segev and M. A. Bandres, "Topological photonics: Where do we go from here?" *Nanophotonics* **10**(1), 425–434 (2020).
15. S. Mittal, G. Moille, K. Srinivasan, *et al.*, "Topological frequency combs and nested temporal solitons," *Nat. Phys.* **17**(10), 1169–1176 (2021).
16. P. St-Jean, V. Goblot, E. Galopin, *et al.*, "Lasing in topological edge states of a one-dimensional lattice," *Nat. Photonics* **11**(10), 651–656 (2017).
17. M. Parto, S. Wittek, H. Hodaei, *et al.*, "Edge-mode lasing in 1D topological active arrays," *Phys. Rev. Lett.* **120**(11), 113901 (2018).
18. H. Zhao, P. Miao, M. H. Teimourpour, *et al.*, "Topological hybrid silicon microlasers," *Nat. Commun.* **9**(1), 981 (2018).
19. Y. Ota, R. Katsumi, K. Watanabe, *et al.*, "Topological photonic crystal nanocavity laser," *Commun. Phys.* **1**(1), 86 (2018).
20. M. A. Bandres, S. Wittek, G. Harari, *et al.*, "Topological insulator laser: Experiments," *Science* **359**(6381), eaar4005 (2018).
21. G. Harari, M. A. Bandres, Y. Lumer, *et al.*, "Topological insulator laser: Theory," *Science* **359**(6381), eaar4003 (2018).
22. D. Smirnova, A. Tripathi, S. Kruk, *et al.*, "Room-temperature lasing from nanophotonic topological cavities," *Light: Sci. Appl.* **9**(1), 127 (2020).
23. Y. Zeng, U. Chattopadhyay, B. Zhu, *et al.*, "Electrically pumped topological laser with valley edge modes," *Nature* **578**(7794), 246–250 (2020).
24. J.-H. Choi, W. E. Hayenga, Y. G. Liu, *et al.*, "Room temperature electrically pumped topological insulator lasers," *Nat. Commun.* **12**(1), 3434 (2021).
25. C. Xu, W. E. Hayenga, D. N. Christodoulides, *et al.*, "Direct modulation of electrically pumped coupled microring lasers," *Opt. Express* **30**(2), 1143–1151 (2022).
26. C. Zhang, D. Liang, G. Kurczveil, *et al.*, "Thermal management of hybrid silicon ring lasers for high temperature operation," *IEEE J. Sel. Top. Quantum Electron.* **21**(6), 385–391 (2015).
27. D. Liang, S. Srinivasan, M. Fiorentino, *et al.*, "A metal thermal shunt design for hybrid silicon microring laser," in *2012 Optical Interconnects Conference*, (IEEE, 2012), 50–51.
28. Lumerical, [Online]. Available: <http://www.lumerical.com>.
29. L. A. Coldren, S. W. Corzine, and M. L. Mashanovitch, *Diode lasers and photonic integrated circuits* (John Wiley & Sons, 2012).
30. E. Gini and H. Melchior, "Thermal dependence of the refractive index of InP measured with integrated optical demultiplexer," *J. Appl. Phys.* **79**(8), 4335–4337 (1996).
31. K. Meradi, F. Tayeboun, S. Ghezali, *et al.*, "Design of a thermal tunable photonic-crystal coupler," *J. Russ. Laser Res.* **32**(6), 572–578 (2011).
32. J. Cui, Q. Miao, P.-a. He, *et al.*, "Temperature dependence of refractive index change for InGaAs/InGaAsP quantum wells," in *Information Optoelectronics, Nanofabrication and Testing*, (Optica Publishing Group, 2012), ITh4A. 24.

33. H.-R. Lee, S.-Y. Lee, T.-Y. Jeong, *et al.*, “Temperature-dependent optical constant of an InGaAsP layer as determined from the reflectance spectrum,” *J. Korean Phys. Soc.* **70**(12), 1064–1069 (2017).
34. Silvaco, [Online]. Available: <https://silvaco.com/>
35. Comsol, [Online]. Available: <https://www.comsol.com/>
36. Comsol, “How to Inspect Your Mesh in COMSOL Multiphysics,” [Online]. Available: <https://www.comsol.com/blogs/how-to-inspect-your-mesh-in-comsol-multiphysics>
37. I. Amelio and I. Carusotto, “Theory of the coherence of topological lasers,” *Phys. Rev. X*. **10**(4), 041060 (2020).
38. M. Secli, M. Capone, and I. Carusotto, “Theory of chiral edge state lasing in a two-dimensional topological system,” *Phys. Rev. Res.* **1**(3), 033148 (2019).
39. R. Bianco and R. Resta, “Mapping topological order in coordinate space,” *Phys. Rev. B* **84**(24), 241106 (2011).
40. S. Arafin, “Electrically-pumped GaSb-based vertical-cavity surface-emitting lasers,” PhD Thesis, Department of Electrical Engineering, Technische Universität München, 2012.